H. Hasegawa[1], T. K. M. Nakamura[2], and R. E. Denton[3]

[1]Institute of Space and Astronautical Science, Japan Aerospace Exploration Agency, Sagamihara, Japan.

[2]Institute of Physics, University of Graz, Graz, Austria.

[3]Department of Physics and Astronomy, Dartmouth College, Hanover, NH, USA.

Corresponding author: Hiroshi Hasegawa (hase@stp.isas.jaxa.jp)

Key Points:

- Method to reconstruct two-dimensional plasma and field structures from spacecraft data based on compressible electron magnetohydrodynamics
- The new method accommodates nonuniform density/temperature, finite electron inertia, and guide magnetic field in the reconnection region
- The new method successfully benchmarked by use of fully kinetic simulation results and applied to a magnetotail reconnection event

Abstract

A method based on electron magnetohydrodynamics (EMHD) for the reconstruction of steady, two-dimensional plasma and magnetic field structures from data taken by a single spacecraft, first developed by Sonnerup et al. (2016), is extended to accommodate inhomogeneity of the electron density and temperature, electron inertia effects, and guide magnetic field in and around the electron diffusion region (EDR), the central part of the magnetic reconnection region. The new method assumes that the electron density and temperature are constant along, but may vary across, the magnetic field lines. We present two models for the reconstruction of electron streamlines, one of which is not constrained by any specific formula for the electron pressure tensor term in the generalized Ohm's law that is responsible for electron unmagnetization in the EDR, and the other is a modification of the original model to include the inertia and compressibility effects. Benchmark tests using data from fully kinetic simulations show that our new method is applicable to both antiparallel and guide-field (component) reconnection, and the electron velocity field can be better reconstructed by including the inertia effects. The new EMHD reconstruction technique has been applied to an EDR of magnetotail reconnection encountered by the Magnetospheric Multiscale spacecraft on 11 July 2017, reported by Torbert et al. (2018) and reconstructed with the original inertia-less version by Hasegawa et al. (2019), which demonstrates that the new method better performs in recovering the electric field and electron streamlines than the original version.

Plain Language Summary

Magnetic reconnection is a physical process that converts magnetic energy to plasma energy by changing the topology of magnetic field lines. Reconnec-

tion occurring at the outer boundary of planetary magnetospheres, called the magnetopause, is key to the entry of solar wind mass and energy into planetary magnetospheres, and reconnection occurring in the nightside portion of the magnetospheres is to fast release of magnetic energy during substorms or sudden auroral brightening. However, space plasma and magnetic field in those reconnection regions are invisible to any remote sensing instruments currently available, and should be measured in situ by spacecraft to understand details of the reconnection process. In the present study, a method for analyzing data from such in-situ measurements, which can visualize two-dimensional magnetic field and electron streamline structures in the central part of the reconnection region, has been improved. The newly developed method allows spatial variations of the electron density and temperature, effects of finite electron mass, and not antiparallel magnetic field configurations in the reconnection region, as commonly observed at the magnetopause, and thus has more applicability. Tests of the method using numerical simulation results and application to actual spacecraft observations demonstrate a better performance than earlier ones.

1 Introduction

A primary objective of the Magnetospheric Multiscale (MMS) mission (Burch et al., 2016), launched in 2016, is to understand the microphysics of magnetic reconnection in the collisionless regime by revealing the kinetic processes occurring in and around the central part of the reconnection region, called the electron diffusion region (EDR), that are responsible for energy conversion, turbulence generation, and particle acceleration through reconnection. To this end, it is necessary to elucidate the connection between the geometrical structure of the EDR and spatiotemporal properties of the kinetic and energy-conversion processes manifested in electron velocity distributions and waves. While in-depth investigation of this connection can be made by simulation studies (e.g., Nakamura et al., 2021), it is not a trivial task to reveal such relations with in-situ measurements. Efforts to obtain information on the geometrical properties have been made by developing data analysis techniques that can reconstruct two- or three-dimensional plasma and/or magnetic field structures from in situ measurements (Sonnerup et al., 2016; Chen et al., 2019; Denton et al., 2020; Torbert et al., 2020).

One type of such reconstruction techniques is based on some physical model, such as electron magnetohydrodynamics (EMHD) (Sonnerup et al., 2016), and is suited for structures that approximately satisfy the model assumptions. It is assumed in the EMHD reconstruction that the structures are approximately two-dimensional (2-D) and time-independent in a proper moving frame, and are described by the incompressible, inertia-less form of the EMHD equations. The original version of the EMHD reconstruction has been successfully applied to MMS observations of a magnetotail reconnection event, reported by Torbert et al. (2018), in which the reconnecting current sheet was symmetric and magnetic fields were nearly antiparallel (Hasegawa et al., 2019), and a magnetopause reconnection event, reported by Burch et al. (2016), in which the current sheet was

weakly asymmetric and the fields were approximately antiparallel (Hasegawa et al., 2017). A weak point of the original EMHD reconstruction is that it is applicable neither to guide-field reconnection (or component merging) because the dissipation term adopted to allow for energy conversion at the X point (Hesse et al., 2011) is specifically for antiparallel reconnection, nor to highly asymmetric reconnection because of the incompressibility (spatially uniform density) assumption. This means that it cannot be applied to most of magnetopause reconnection events in which both the guide magnetic field (field component along the X-line direction) and density jump across the current sheet are often significant (Burch & Phan, 2016).

Some of the above assumptions made in the original EMHD reconstruction have been relaxed in a recent work by Korovinskiy et al. (2021), allowing for reconstruction with electron inertia and guide-field effects taken into account, but with an additional assumption on the electron velocity field. However, their model still assumes electron incompressibility (uniform electron density, i.e., $n_e = \text{const.}$), and we find their assumption on the velocity field, or equivalently, on the magnetic field component B_z along the direction of negligible gradient ($\frac{\partial}{\partial z} \approx 0$) to be not well satisfied in and around the EDR (Appendix). In the present study, we present a novel model in the EMHD framework for the reconstruction of the EDR with electron compressibility, inertia, and guide-field effects all incorporated. Our model was inspired by a recent study by Korovinskiy et al. (2020), showing that in 2-D antiparallel reconnection, the electron density and temperature are both roughly preserved along the magnetic field in the reconnection plane (see their Figures 3 and 4).

The paper is organized as follows. Section 2 presents theory developed for the new version of the EMHD reconstruction. Section 3 describes the actual numerical procedures taken in the reconstruction. Section 4 provides benchmark tests of the new EMHD reconstruction by use of data from fully kinetic simulations of both antiparallel and guide-field magnetic reconnection. Section 5 presents first results of the new reconstruction applied to the EDR of magnetotail reconnection observed by MMS on 11 July 2017, previously analyzed by Torbert et al. (2018) and Hasegawa et al. (2019). Summary and discussion are given in section 6, and Appendix provides some discussions on the assumptions made in the present study and in Korovinskiy et al. (2021), along with key differences between the two studies.

2 Theory

We follow the same steps as taken by Sonnerup et al. (2016) (hereafter referred to as S16) but for compressible electrons with finite inertia. Some parts are repeated, because those would be helpful to better understand the improvements made in the present study.

2.1 Description of Fields and Flows

We assume a steady ($\frac{\partial}{\partial t} = 0$), 2-D ($\frac{\partial}{\partial z} = 0$) geometry in and close to the EDR where ion dynamics can be neglected. The electron number density and velocity

are defined as $n_e \equiv n$ and $\mathbf{v}_e \equiv \mathbf{v}$, respectively. The time-independnet form of the continuity equation $\nabla \bullet (n\mathbf{v}) = 0$ for electrons allows for the use of the compressible stream function ψ (Sonnerup et al., 2006). The electron number flux as well as the magnetic field can then be defined as

$$n\mathbf{v} = \nabla\psi \times \hat{\mathbf{z}} + n(x,y)v_z(x,y)\hat{\mathbf{z}}, \quad (1)$$

$$\mathbf{B} = \mathbf{B}_\perp + B_z\hat{\mathbf{z}} = \nabla A \times \hat{\mathbf{z}} + B_z(x,y)\hat{\mathbf{z}}, \quad (2)$$

$$\mu_0\mathbf{j} = \nabla B_z \times \hat{\mathbf{z}} - \hat{\mathbf{z}}\nabla^2 A = -\mu_0 \mathrm{ne}\mathbf{v}, \quad (3)$$

where the partial magnetic vector potential is $A_z \equiv A$, and $\mathbf{j}$ is the electron current density. From (1) and (3), it follows that the axial component of the magnetic field is equivalent to the compressible stream function via $B_z = -\mu_0 \mathrm{e}$.

2.2 Ohm's Law

The time-independent form of the electron momentum equation (i.e., the generalized Ohm's law) is

$$nm_e\mathbf{v}\bullet\nabla\mathbf{v} = -\nabla\bullet\mathbf{P} - ne(\mathbf{E} + \mathbf{v} \times \mathbf{B}). \quad (4)$$

In this expression, we can write $\mathbf{v} = \mathbf{v}_\perp + v_z\hat{\mathbf{z}} = \frac{-(\nabla B_z \times \hat{\mathbf{z}})}{(\mu_0 ne)} + v_z\hat{\mathbf{z}}$, and $\mathbf{E} = -\nabla\phi(x,y) + E_{z0}\hat{\mathbf{z}}$, where the axial component of the electric field E_{z0} should be constant for steady structures when seen in the frame comoving with the structure. The reconnection electric field may be defined as $E_0 = V_\infty B_\infty = \frac{E_{z0}j_z}{|j_z|}$, where V_∞ is the upstream electron flow velocity toward the current sheet and B_∞ is the upstream in-plane field intensity (see Figure 1 of S16). After some vector algebra, the inertia term in (4) becomes

$$nm_e\mathbf{v}\bullet\nabla\mathbf{v} = nm_e\left[\frac{\nabla v_\perp^2}{2} - \mathbf{v}_\perp \times (\nabla \times \mathbf{v}_\perp) + \hat{\mathbf{z}}\mathbf{v}_\perp\bullet\nabla v_z\right]$$

$$= nm_e\left[\frac{\nabla v_\perp^2}{2} - \left(\frac{1}{(\mu_0 ne)^2}\right)\left\{\nabla^2 B_z - \nabla ln(n)\bullet\nabla B_z\right\}\nabla B_z + \hat{\mathbf{z}}\left(\mathbf{v}_\perp\bullet\nabla\right)v_z\right], \quad (5)$$

where $\nabla \times \mathbf{v}_\perp = \left(\frac{1}{(\mu_0 ne)}\right)\left[\nabla^2 B_z - \nabla ln(n)\bullet\nabla B_z\right]\hat{\mathbf{z}}$ is used to reach the final form. As in S16, we assume that the electron pressure tensor can be written in the form

$$\nabla\bullet\mathbf{P} = \nabla\tilde{p}(x,y) + \hat{\mathbf{z}}f(x,y). \quad (6)$$

We also note that the Lorentz force term can be written as

$$-ne\left(\mathbf{v} \times \mathbf{B}\right) = \mathbf{j} \times \mathbf{B} = \left(\frac{1}{\mu_0}\right)\left[-\frac{\nabla B_z^2}{2} + \hat{\mathbf{z}}\mathbf{B}_\perp\bullet\nabla B_z - \left(\nabla^2 A\right)\nabla A\right], \quad (7)$$

where the axial component of the electron convection electric field is defined by Korovinskiy et al. (2020) as

$$\varepsilon^* = -\left(\mathbf{v}_\perp \times \mathbf{B}_\perp\right)_z = \left(\frac{1}{(\mu_0 ne)}\right)\mathbf{B}_\perp\bullet\nabla B_z. \quad (8)$$

Then Ohm's law can be rearranged to become

$$E_{z0}\hat{\mathbf{z}} - \nabla\phi = \left(\frac{1}{(\mu_0 \mathrm{ne})}\right)\left[-\frac{\nabla B_z^2}{2} + \hat{\mathbf{z}}\mathbf{B}_\perp \bullet \nabla B_z - \left(\nabla^2 A\right)\nabla A\right] - \frac{\left(\nabla\tilde{p} + \hat{\mathbf{z}} f(x,y)\right)}{(\mathrm{ne})}$$

$$+ \left(\tfrac{m_e}{e}\right)\left[-\tfrac{\nabla v_\perp^2}{2} - \hat{\mathbf{z}}\left(\mathbf{v}_\perp \bullet \nabla\right) v_z + \left(\tfrac{1}{(\mu_0 \mathrm{ne})^2}\right)\left\{\nabla^2 B_z - \nabla \ln(n) \bullet \nabla B_z\right\}\nabla B_z\right]. \quad (9)$$

The in-plane components of Ohm's law give

$$-\nabla\phi = \left(\frac{1}{(\mu_0 \mathrm{ne})}\right)\left[-\frac{\nabla B_z^2}{2} - \left(\nabla^2 A\right)\nabla A\right] - \frac{\nabla\tilde{p}}{(\mathrm{ne})}$$

$$+ \left(\tfrac{m_e}{e}\right)\left[-\tfrac{\nabla v_\perp^2}{2} + \left(\tfrac{1}{(\mu_0 \mathrm{ne})^2}\right)\left\{\nabla^2 B_z - \nabla \ln(n) \bullet \nabla B_z\right\}\nabla B_z\right]. \quad (10)$$

Multiplying (10) by the density, we arrive at

$$\nabla\left[-n\phi + \frac{\tilde{p}}{e} + \left(\frac{1}{(\mu_0 e)}\right)\frac{B_z^2}{2} + \left(\frac{\mathrm{nm}_e}{e}\right)\frac{v_\perp^2}{2}\right] = \left[-\phi + \left(\frac{m_e}{e}\right)\frac{v_\perp^2}{2}\right]\nabla n$$
$$- \left(\tfrac{1}{(\mu_0 e)}\right)\left(\nabla^2 A\right)\nabla A \; + \; \left(\tfrac{1}{(\mu_0 e)^2}\right)\left(\tfrac{m_e}{(\mathrm{ne})}\right)\left[\nabla^2 B_z - \nabla \ln(n) \bullet \nabla B_z\right]\nabla B_z. \quad (11)$$

The three terms on the right-hand side that do not have the appearance of perfect gradients must together form a perfect gradient of some function $G\left(A, B_z, n\right)$:

$$\nabla G = \left[-\phi + \left(\frac{m_e}{e}\right)\frac{v_\perp^2}{2}\right]\nabla n - \left(\frac{1}{(\mu_0 e)}\right)\left(\nabla^2 A\right)\nabla A$$
$$+ \left(\tfrac{1}{(\mu_0 e)^2}\right)\left(\tfrac{m_e}{(\mathrm{ne})}\right)\left[\nabla^2 B_z - \nabla \ln(n) \bullet \nabla B_z\right]\nabla B_z. \quad (12)$$

We then find from (11) that

$$K = n\phi - \tfrac{\tilde{p}}{e} - \left(\tfrac{1}{(2\mu_0 e)}\right)B_z^2 - \left(\tfrac{\mathrm{nm}_e}{(2e)}\right)v_\perp^2 + G \quad (13)$$

is a global constant, and we can take $K = 0$ to compute G along the spacecraft path and at each integration step.

Here we assume that the electron density and pressure are functions of A alone, $n(x,y) = n(A)$, and $\tilde{p}(x,y) = \tilde{p}(A)$, which are approximately satisfied in the vicinity of the EDR (Korovinskiy et al., 2020). By use of $\nabla n = \left(\frac{dn(A)}{\mathrm{dA}}\right)\nabla A$, we can expand (12) in the form $\nabla G\left(A, B_z\right) = \left(\frac{\partial G}{\partial A}\right)\nabla A + \left(\frac{\partial G}{\partial B_z}\right)\nabla B_z$, so that

$$\tfrac{\partial G}{\partial A} = \left[-\phi + \left(\tfrac{m_e}{e}\right)\tfrac{v_\perp^2}{2}\right]\left(\tfrac{dn(A)}{\mathrm{dA}}\right) - n v_z, \quad (14)$$

$$\tfrac{\partial G}{\partial B_z} = \left(\tfrac{1}{(\mu_0 e)^2}\right)\left(\tfrac{m_e}{(\mathrm{ne})}\right)\left[\nabla^2 B_z - \nabla \ln(n) \bullet \nabla B_z\right], \quad (15)$$

where a Grad-Shafranov (GS) equation $\nabla^2 A = \mu_0 \mathrm{n} e v_z$ (axial component of (3)) is used to reach (14).

We now turn to the axial component of Ohm's law (9)

$$\frac{f(x,y)}{(\mathrm{ne})} = -E_{z0} + \left(\frac{1}{(\mu_0 \mathrm{ne})}\right) \mathbf{B}_\perp \bullet \nabla B_z - \left(\frac{m_e}{e}\right) (\mathbf{v}_\perp \bullet \nabla)\, v_z. \quad (16)$$

With (8), noting that $(\mathbf{v}_\perp \bullet \nabla) = -(\mathbf{v}_\perp \times \mathbf{B}_\perp)_z \frac{\partial}{\partial A} = \varepsilon^* \frac{\partial}{\partial A}$ (see Eq. (21) of Korovinskiy et al. (2020)), it follows that

$$\frac{f(x,y)}{(\mathrm{ne})} = -E_{z0} + \varepsilon^* \left[1 - \left(\frac{m_e}{e}\right) \frac{\partial v_z}{\partial A}\right]. \quad (17)$$

It is seen from (17) that the electron inertia contribution to the reconnection electric field E_0 can be assessed by the term $-\varepsilon^* \left(\frac{m_e}{e}\right) \frac{\partial v_z}{\partial A}$; whether it positively or negatively contributes to E_0 depends on the sign of $\frac{\partial v_z}{\partial A}$, given that $\varepsilon^* = -(\mathbf{v}_\perp \times \mathbf{B}_\perp)_z$ has the same sign as E_{z0} everywhere around the reconnection site. In the case when E_{z0} is negative, as in Figure 1 of S16, so that ε^* is also negative, A has a larger value in the inflow than in the outflow region. As electrons in the inflow region are advected across the transverse magnetic field $\mathbf{B}_\perp$ toward the EDR, moving to a smaller A region, they are accelerated along the direction opposite to the reconnection electric field (along $+\hat{\mathbf{z}}$) and thus v_z increases, making $\frac{\partial v_z}{\partial A}$ negative. In such regions, the above inertia term makes a positive contribution to E_0. On the other hand, in the outflow region v_z (electron current intensity) generally decreases with distance from the X point in the outflow direction, so that $\frac{\partial v_z}{\partial A}$ is positive. The inertia term then makes a negative contribution to E_0. This picture is consistent with 2-D kinetic simulations of magnetic reconnection (Divin et al., 2012; Egedal et al., 2019).

3 Reconstruction Procedure

Our new reconstruction method requires as input magnetic field, electric field, and electron moment data taken by a single spacecraft during a properly selected interval, while electric field data are not necessarily required in the original EMHD method (S16). The coordinate system (the invariant axis orientation $\hat{\mathbf{z}}$, and velocity of the frame in which the structure is seen to be time-stationary) for the reconstruction can be estimated by single- or multi-spacecraft methods, as reviewed by Shi et al. (2019), with successful applications to MMS observations of both magnetopause and magnetotail current sheets (Denton et al., 2016, 2018, 2021).

The magnetic vector potential A, stream function ψ, and electrostatic potential ϕ on the x axis, defined as the projection of the spacecraft path onto the plane perpendicular to $\hat{\mathbf{z}}$, can be obtained by $A(x,0) = \int \left(\frac{\partial A}{\partial x}\right) dx = -\int B_y(x,0)dx$, $\psi(x,0) = \int \left(\frac{\partial \psi}{\partial x}\right) dx = -\int n(x,0) v_y(x,0) dx$, and $\phi(x,0) = \int \left(\frac{\partial \phi}{\partial x}\right) dx = -\int E_x(x,0)dx$, respectively. Since magnetic field data are generally more reliable than electron moment data, we use measured B_z to set the initial condition for ψ via $B_z = -\mu_0 \mathrm{e}$, rather than the y component of the electron flux integrated in the x direction. In the following three subsections,

we describe how the actual reconstruction, namely, integration along y of A, B_z (equivalent to ψ), and ϕ is conducted.

3.1 Reconstruction of the Transverse Magnetic Field

We assume that the z component of the current density is a function of A only so that the GS equation is

$$\nabla^2 A = -\mu_0 j_z(A) = \mu_0 e n(A) v_z(A), \quad (18)$$

because this assumption is roughly satisfied in the reconnection region (Figure A1 in Appendix), and allows for a sufficiently good reconstruction of the transverse magnetic field (Sonnerup et al., 2016; Hasegawa et al., 2017, 2019; Korovinskiy et al., 2020, 2021). The functional forms of $n(A)$ and $v_z(A)$ (and also $\tilde{p}(A)$) can be determined by polynomial or exponential fitting to the data taken during an analysis interval. The reconstruction of A is done in a similar way to the classical GS reconstruction (Hau & Sonnerup, 1999), i.e., $A(x, y \pm \Delta y) = A(x, y) \pm \Delta y B_x(x, y) + \left(\frac{(\Delta y)^2}{2}\right) \frac{\partial^2 A}{\partial y^2}$, in which $\frac{\partial^2 A}{\partial y^2}$ is computed from (18). Likewise, the reconstruction of B_x can be done by use of $\frac{\partial B_x}{\partial y} = \frac{\partial^2 A}{\partial y^2}$. Once the 2-D map of A is obtained, those for n, v_z, and $\tilde{p}$ can also be constructed from the corresponding functions of A.

3.2 Reconstruction of the Axial Magnetic Field Component

The reconstruction of the z component of the magnetic field B_z, equivalent to that of the compressible stream function ψ, requires $\frac{\partial^2 B_z}{\partial y^2}$ to be obtained at each step of integration along y. It also involves the reconstruction of v_x by use of

$$\frac{\partial v_x}{\partial y} = \frac{\partial}{\partial y}\left[-\frac{1}{\mu_0 \mathrm{en}} \frac{\partial B_z}{\partial y}\right] = -\frac{1}{\mu_0 \mathrm{en}} \frac{\partial^2 B_z}{\partial y^2} - v_x \frac{\partial \ln(n)}{\partial y}. \quad (19)$$

We discuss two possibilities to perform this integration.

3.2.1 Case 1: General case with no requirement for $f(x, y)$

We make use of the following relation

$$\frac{\partial G\,(A, B_z)}{\partial x} = \left(\frac{\partial G}{\partial A}\right) \frac{\partial A}{\partial x} + \left(\frac{\partial G}{\partial B_z}\right) \frac{\partial B_z}{\partial x}$$

$$= \left(\tfrac{\partial G}{\partial A}\right)(-B_y) + \left(\tfrac{\partial G}{\partial B_z}\right)(\mu_0 \mathrm{en} v_y) \quad (20)$$

Substituting (15) into (20), it follows that

$$\nabla^2 B_z = \nabla \ln(n) \bullet \nabla B_z + \left(\frac{\mu_0 e^2}{m_e}\right) \frac{1}{v_y} \left(\frac{\partial G}{\partial x} + B_y \frac{\partial G}{\partial A}\right) \quad (21)$$

where $\frac{\partial G}{\partial A}$ can be computed from (14), $\frac{\partial n}{\partial y} = \left(\frac{dn(A)}{\mathrm{dA}}\right)\left(\frac{\partial A}{\partial y}\right) = \left(\frac{dn(A)}{\mathrm{dA}}\right) B_x$, and $\frac{\partial B_z}{\partial y} = -\mu_0 \mathrm{en} v_x$. Note that the B_z reconstruction using (21) does not require any specific expression for the axial component of the electron pressure tensor term $f(x, y)$. The B_z reconstruction can be performed by use of $B_z(x, y) \pm$

$\Delta y \frac{\partial B_z}{\partial y} + \left(\frac{(\Delta y)^2}{2}\right) \frac{\partial^2 B_z}{\partial y^2}$, in which (21) is used to compute $\frac{\partial^2 B_z}{\partial y^2}$. However, the second term on the right-hand side of (21) has v_y in the denominator, so that the B_z integration may encounter numerical problems in the region where $|v_y|$ is small. In such regions or for specific boundary conditions, the following expression for $f(x, y)$ may be used.

3.2.2 Case 2: Hesse-Kuznetsova dissipation term

For near antiparallel reconnection, Hesse et al. (2011) shows that the part of the electron pressure tensor term due to nongyrotropic electrons can be modeled as follows,

$$f(L, N) = n \frac{\partial v_L}{\partial L} \sqrt{2 m_e k T_e}, \quad (22)$$

where the LMN coordinate system is used, so that the L axis is directed along the local tangent to the current sheet, with $\frac{\partial}{\partial M} = -\frac{\partial}{\partial z} = 0$. Following the same approach as taken by Sonnerup et al. (2016) (Eqs. (19-23) in S16), but including the compressibility effect, we arrive at

$$f(x, y) = -\frac{\sqrt{2 m_e k T_e}}{\mu_0 e} \left[(cos2\theta) \frac{\partial^2 B_z}{\partial x \partial y} + \frac{1}{2} (sin2\theta) \left\{ \frac{\partial^2 B_z}{\partial y^2} - \frac{\partial^2 B_z}{\partial x^2} + \mu_0 e \left(\frac{\partial n}{\partial x} v_y + \frac{\partial n}{\partial y} v_x \right) \right\} + \mu_0 e \left(\cos^2 \theta \frac{\partial n}{\partial x} v_x + s \right.$$
(23)

where the L axis is rotated counterclockwise about the z axis by an angle θ (see Figure 1 of S16). Thus (17) becomes

$$\frac{\sqrt{2 m_e k T_e}}{\mu_0 n e^2} \left[(cos2\theta) \frac{\partial^2 B_z}{\partial x \partial y} + \frac{1}{2} (sin2\theta) \left\{ \frac{\partial^2 B_z}{\partial y^2} - \frac{\partial^2 B_z}{\partial x^2} + \mu_0 e \left(\frac{\partial n}{\partial x} v_y + \frac{\partial n}{\partial y} v_x \right) \right\} + \mu_0 e \left(\cos^2 \theta \frac{\partial n}{\partial x} v_x + \sin^2 \theta \frac{\partial n}{\partial y} v_y \right) \right.$$
$$E_{z0} - \varepsilon^* \left[1 - \frac{m_e}{e} \frac{\partial v_z}{\partial A} \right], \quad (24)$$

where $\frac{\partial^2 B_z}{\partial x \partial y} = \frac{\partial (-\mu_0 e n v_x)}{\partial x} = -\mu_0 e n \left[v_x \frac{\partial \ln(n)}{\partial x} + \frac{\partial v_x}{\partial x} \right]$. Provided that E_{z0}, which is assumed constant, is known, $\frac{\partial^2 B_z}{\partial y^2}$ can be computed from (24) at each integration step, from which we can get $\nabla^2 B_z$ as well. The average of the axial component of the measured electric field in the structure frame can be used as E_{z0}. Alternatively, when multi-spacecraft information is available, the E_{z0} value may be optimized as a free parameter in such a way that the correlation coefficient is maximized between the field and electron velocity components measured by spacecraft not used in the reconstruction and those predicted from the field maps along the paths of the spacecraft, as implemented by Hasegawa et al. (2017).

3.3 Reconstruction of G and the electrostatic potential ϕ

We make use of the following relation

$$\frac{\partial G(A, B_z)}{\partial y} = \left(\frac{\partial G}{\partial A} \right) \frac{\partial A}{\partial y} + \left(\frac{\partial G}{\partial B_z} \right) \frac{\partial B_z}{\partial y}$$
$$= \left(\frac{\partial G}{\partial A} \right) B_x + \left(\frac{\partial G}{\partial B_z} \right) (-\mu_0 e n v_x) \quad (25)$$

Since $\frac{\partial G}{\partial A}$ and $\frac{\partial G}{\partial B_z}$ can be computed by (14) and (15), respectively, (25) can be used to integrate G in the y direction. The electrostatic potential ϕ can then be computed by use of (13). In Case 1 with no electron pressure tensor model, $\frac{\partial G}{\partial B_z}$ can be directly computed from substituting (14) into (20).

4 Test with Simulation Data

4.1 Reconstruction of Antiparallel Reconnection

We apply our new EMHD reconstruction code with electron compressibility and inertia effects to synthetic data from a 2-D fully kinetic simulation of symmetric, antiparallel reconnection, as used by S16. See Nakamura et al. (2016) for details of the settings of the particle-in-cell (PIC) simulation, and S16 for the path in the simulation box of a synthetic spacecraft making virtual observations and how physical quantities are normalized. Note that the data used to initiate the reconstruction were taken from a simulation phase in which the field configuration appeared approximately steady. See Text S1 in the Supporting Information for the normalized forms of the equations used in the new EMHD reconstruction.

Figure 1 shows the quantities (v_z, n, and $\tilde{p}$) from the virtual observations, which are assumed in the reconstruction to be functions of A only, plotted against the vector potential A computed along the spacecraft path. The path is similar to the one in Figure 5 of S16 with the angle between the x axis and the current sheet plane set at $\theta \sim 20^\circ$, except that the X point is now set to be located at $(x, y) = (12, -2)\lambda_{e0}$ in the reconstruction coordinate system (see Figure 2). Here the electron inertial length $\lambda_{e0} = \left(\frac{m_e}{(\mu_0 n_0 e^2)}\right)^{\frac{1}{2}}$, where the density at the center of the initial Harris-type current sheet is $n_0 + n_\infty$, with the density outside the current sheet n_∞ and $\frac{n_0}{n_\infty} = 5$. Overall, all the quantities increase toward the center of the reconnecting current sheet, as expected (larger A values correspond to the inflow regions, and smaller values to the current sheet center). It is seen that those quantities can be roughly expressed by single exponentials (thick curves). We have also tested fitting by polynomial functions, but find that reconstruction errors, as discussed in the following paragraphs, are larger in this particular case.

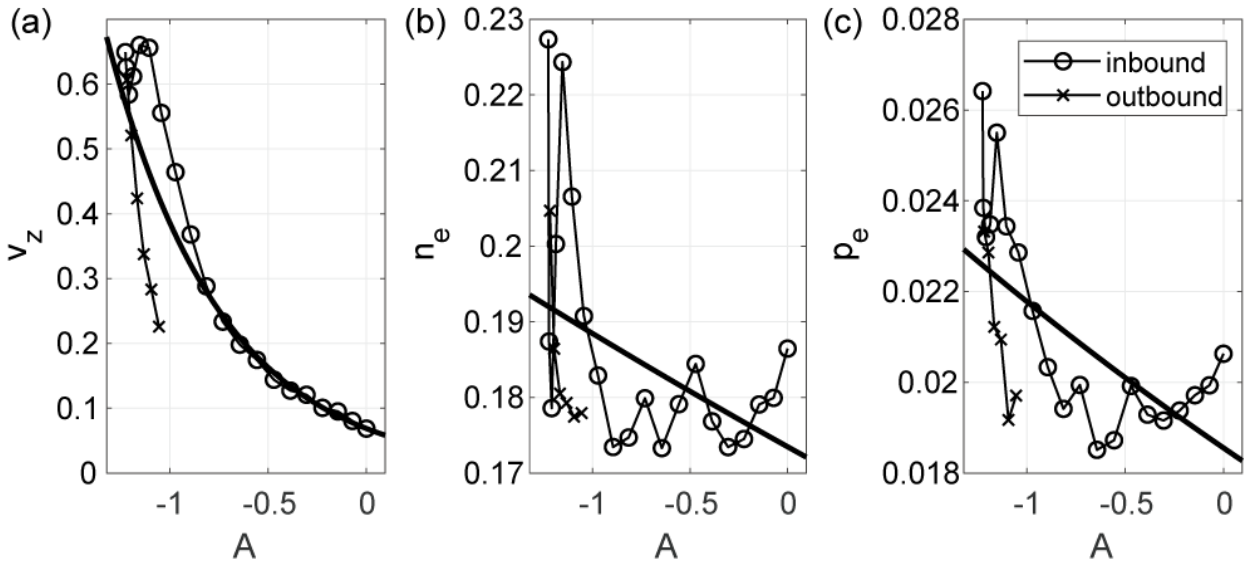

Figure 1. (a) Axial component of the electron velocity v_z, (b) electron density, and (c) electron pressure (average of the three diagonal components of the electron pressure tensor), plotted as a function of partial vector potential A based on virtual spacecraft observations in a fully kinetic simulation of symmetric, antiparallel reconnection (S16). Circles and crosses are data from the path toward (inbound) and away from (outbound) the center of the current sheet, respectively. Thick curves are exponential fits to the data.

Figure 2 shows a comparison of the field maps reconstructed from the new EMHD code with the simulation results. A combination of Case 1 and Case 2 (Hesse-Kuznetsova dissipation term) is used to reconstruct B_z, in which Case 1 is used in the part of the reconstruction domain where $|v_y| > 0.01$ (this parameter should be adjusted by trial and error for each event application) while Case 2 is used in the other parts (see section 3.2 for details). Since our analysis of the simulation results shows that $\nabla^2 B_z$ is significant only in the region near the center of the current sheet, $\nabla^2 B_z = 0$ is imposed in the part of the reconstruction domain where the intensity of the transverse magnetic field $B_\perp$ exceeds a threshold value (see Appendix for details). The comparison shows that A, B_z, and ϕ are all well reconstructed, with large errors only around some of the four corners of the reconstruction domain (Figures 2c, 2f, and 2i). Figure 2e, in particular, shows that the inflow and outflow pattern of the electron flows is well recovered, with a stagnation point close to the expected location $(x, y) = (12, -2)\lambda_{e0}$. The bottom two sets of panels shows that the tendency that the density and pressure are both high near the current sheet center is recovered, although small-scale features are not very well recovered because of the model assumptions (n and $\tilde{p}$ preserved along the transverse field lines).

Figure 3 shows a comparison of errors for A, B_z, and ϕ from a few variants of the

EMHD reconstruction as a function of y, in which the same initial conditions are used. See Figures S1-S3 for reconstruction results and corresponding error maps from the three incompressible versions ("S16", "in,Case-2 only", and "in,Case-1&2") in which the density and pressure are set at constant values. Since even at an equal y location the errors have different values at different x locations, the first quartile, median, and third quartile of the errors are shown in the left, middle, and right panels, respectively. As expected, the errors generally increase with distances from the spacecraft path ($y = 0$) where the initial conditions are set. The error in the electrostatic potential ϕ for S16 is not zero even at $y = 0$, because electric field data are not used to reconstruct ϕ in S16 (ϕ is computed from Eq. (25) in S16).

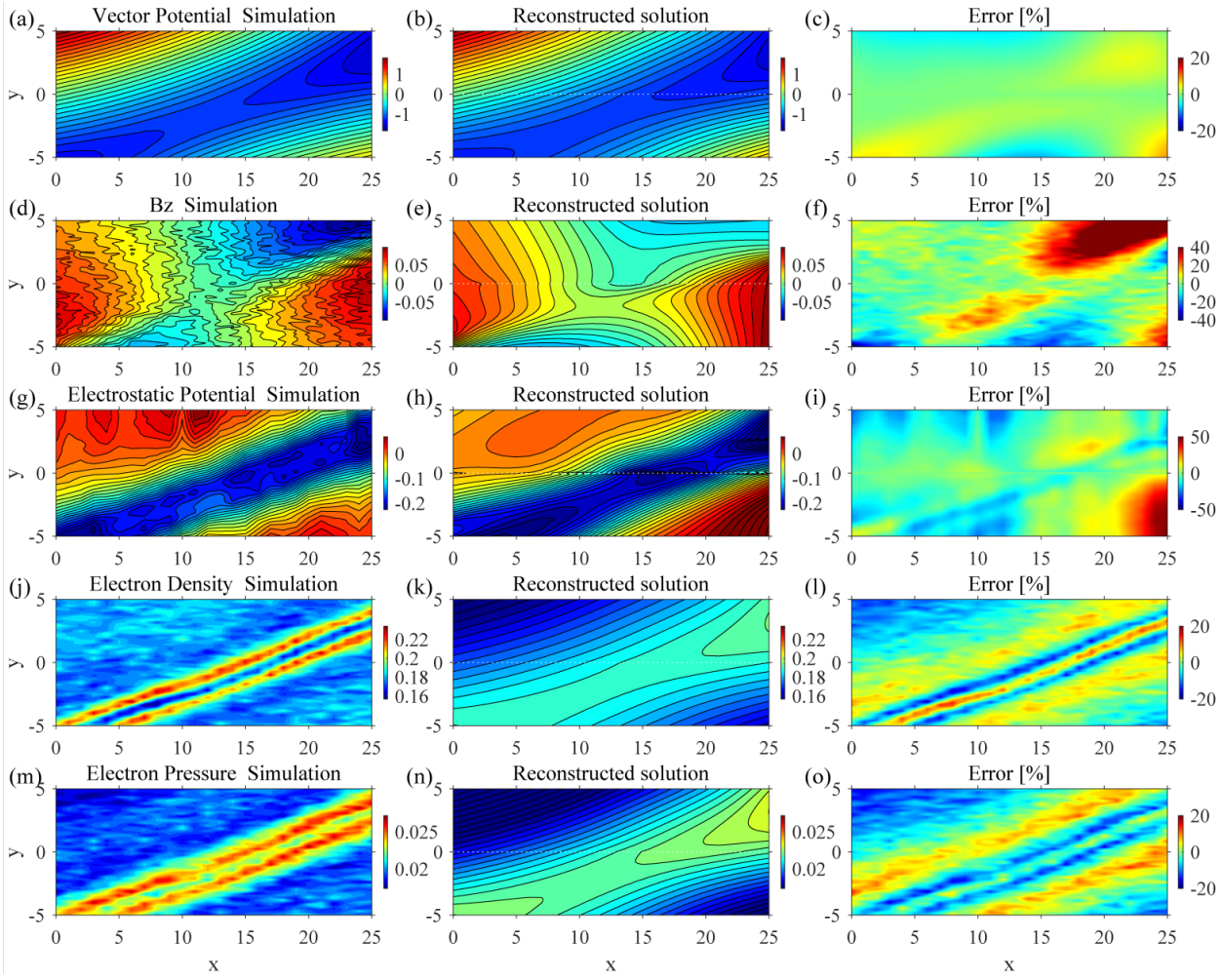

Figure 2. Results from the compressible EMHD reconstruction with electron inertia, compared with the PIC simulation results. The left panels show simula-

tion values in the reconstruction domain: (a) magnetic vector potential A, (d) axial magnetic field component B_z, equivalent to the electron stream function ψ, (g) electrostatic potential ϕ, (j) electron density n, and (m) electron pressure $\tilde{p}$. The middle column shows the corresponding reconstructed solutions, with the path of the virtual spacecraft along $y = 0$. Errors in the right panels are in % of the maximum magnitude of the simulated values in the reconstruction domain.

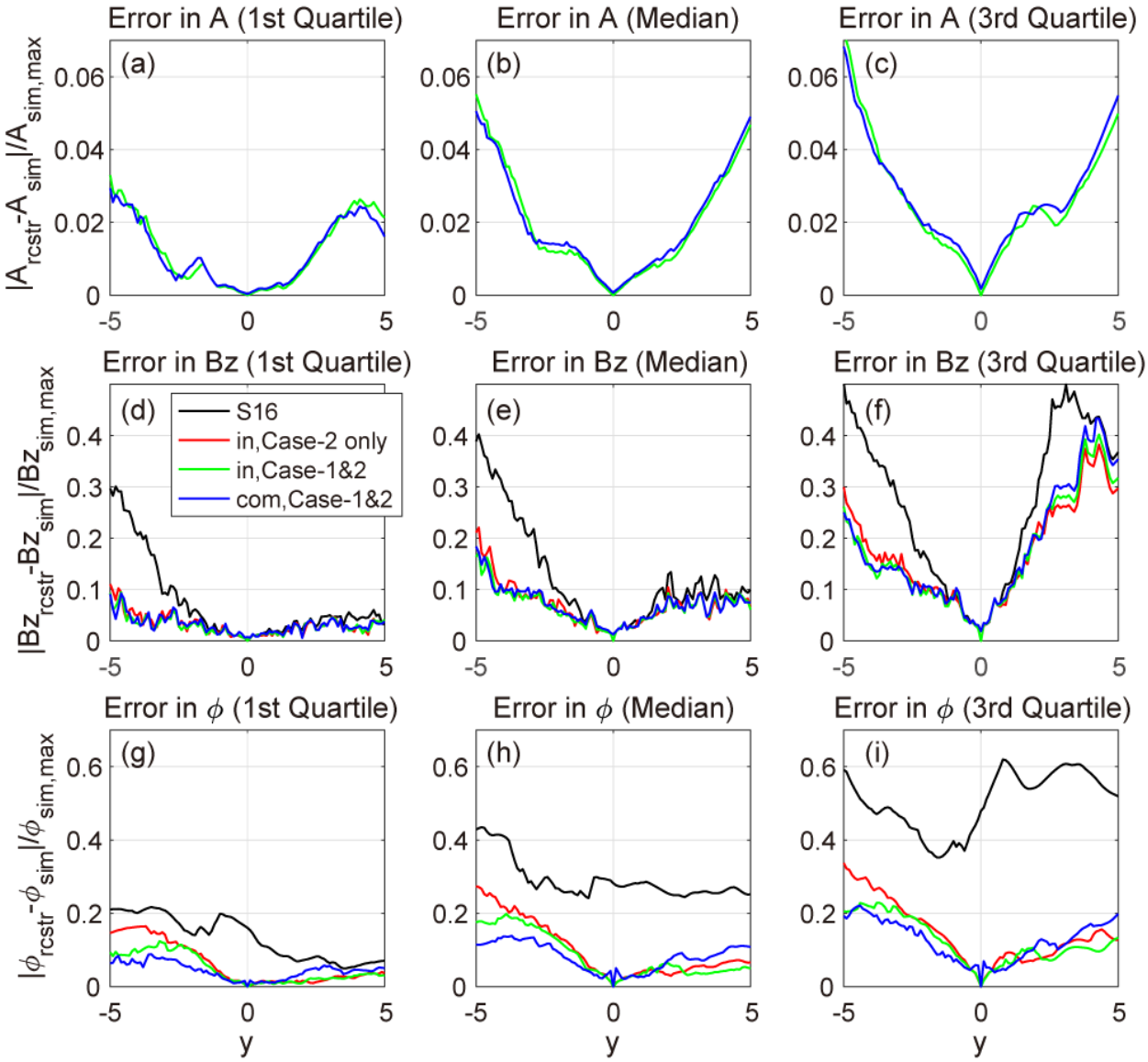

Figure 3. Comparison of errors as a function of y among four versions of the

EMHD reconstruction. "S16" stands for the incompressible inertia-less version, originally developed by S16, "in" for the incompressible version with finite inertia, and "com" for the compressible version with finite inertia. See section 3.2 for how B_z is reconstructed in Case-1 and Case-2. The errors for the results in Figure 2 are shown by blue curves.

The top panels of Figure 3 show that the A errors are comparable between the incompressible and compressible versions. All the three incompressible versions have the same solution and thus the same errors for A. We also note that the A errors in the present S16 case are smaller than those from the original S16 code because we find that the errors can be reduced by using the $\frac{\partial^2 A}{\partial y^2}$ value at the previous integration step in y if the $\frac{\partial^2 A}{\partial y^2}$ magnitude exceeds a threshold (~0.5 in the normalized unit), i.e., by avoiding very large values of $\left|\frac{\partial^2 A}{\partial y^2}\right|$. On the other hand, the middle and bottom panels show that both B_z and ϕ errors are significantly smaller for the new versions incorporating electron inertia effects than the inertia-less (S16) version. Since the constraint of $\nabla^2 B_z = 0$ in the regions away from the current sheet (see Appendix) is used in the present S16 as well as new versions (while it was not used in the results reported by S16), the improvement in the B_z and ϕ reconstructions is exclusively due to incorporating the inertia terms. While the B_z errors are comparable among the three finite-inertia versions (Figures 3d-3f), the ϕ errors for the compressible version are smaller in the negative y region and appear more symmetric with respect to $y = 0$ than for the incompressible versions. In summary, one may conclude that although no particular version is better than all the others in reconstructing all quantities, the most general version with both compressibility and inertia effects, as shown in Figure 2, performs best as a whole.

4.2 Reconstruction of Guide-field Reconnection

We now apply our new EMHD reconstruction code to data from a PIC simulation of symmetric, guide-field reconnection. The simulation settings are the same as for antiparallel reconnection, as shown in Figures 1-3, except that the guide field is set equal to the reconnecting field component. The path of the synthetic spacecraft observations is the same as in the antiparallel reconnection case, as shown in Figure 4a, with the X point at $(x, y) = (12, -2)\lambda_{e0}$ in the reconstruction plane. Figures 4c-4f show input values of the magnetic and electric fields and electron velocity, density, and pressure taken from the virtual observations. Since the spacecraft did not encounter the inflow region on the negative-N side of the current sheet (Figure 4a), A continuously decreases along the path from zero to a minimum in the outflow region (Figure 4b), with a v_z peak near the X point (Figures 4b and 4e). See Pritchett & Coroniti (2004) and Le et al. (2010) for general properties of guide-field reconnection in PIC simulations.

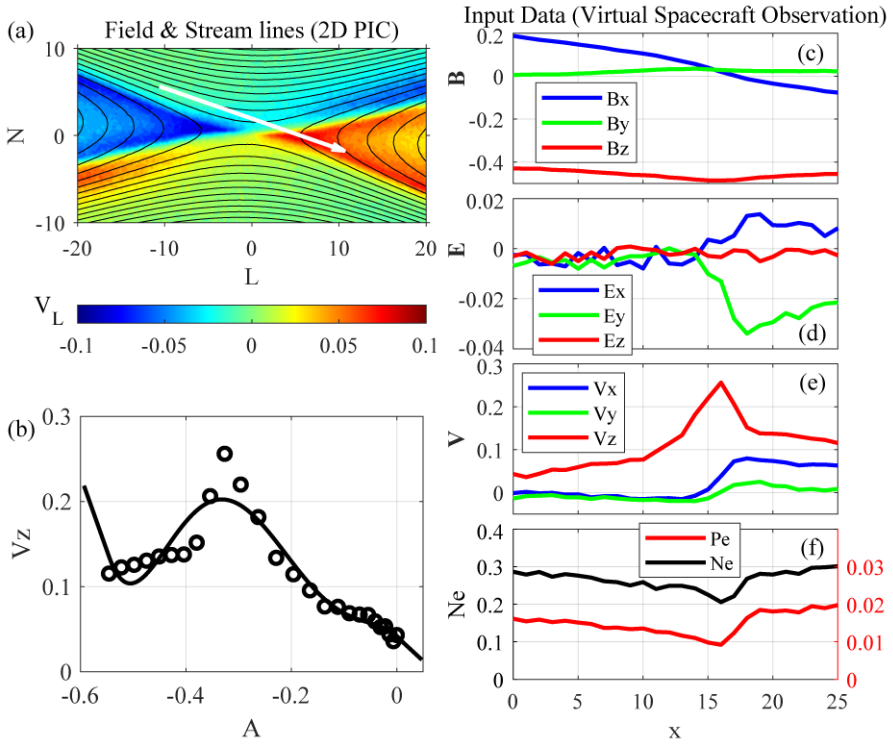

Figure 4. Data used to initiate the reconstruction of guide-field reconnection. (a) Magnetic field geometry from the PIC simulation, with the L component of the electron velocity v_x in color and spacecraft path indicated by the white arrow. (b) Axial component of the electron velocity v_z versus magnetic vector potential A based on the virtual spacecraft observations. The thick curve is a 5th-order polynomial fit to the data, used in the A and v_z reconstructions. (c) Three components in the reconstruction coordinate system of the magnetic field, (d) electric field, (e) electron velocity, and (f) electron density and pressure taken along the path.

Figure 5 shows the reconstruction results from the incompressible, finite-inertia version compared with the simulation results. The top and middle panels show that the transverse field lines and electron streamlines, respectively, are well reconstructed, although the A errors are large around the two upper corners of the reconstruction domain and the reconstructed electron flow pattern is not as asymmetric as seen in the simulation. The bottom panels show that the ϕ errors are substantial around the two upper corners but small at small $|y|$ regions. Importantly, a quadrupolar electrostatic potential pattern seen in the simulation result (Figure 5g) is roughly recovered in the reconstructed $\phi(x, y)$.

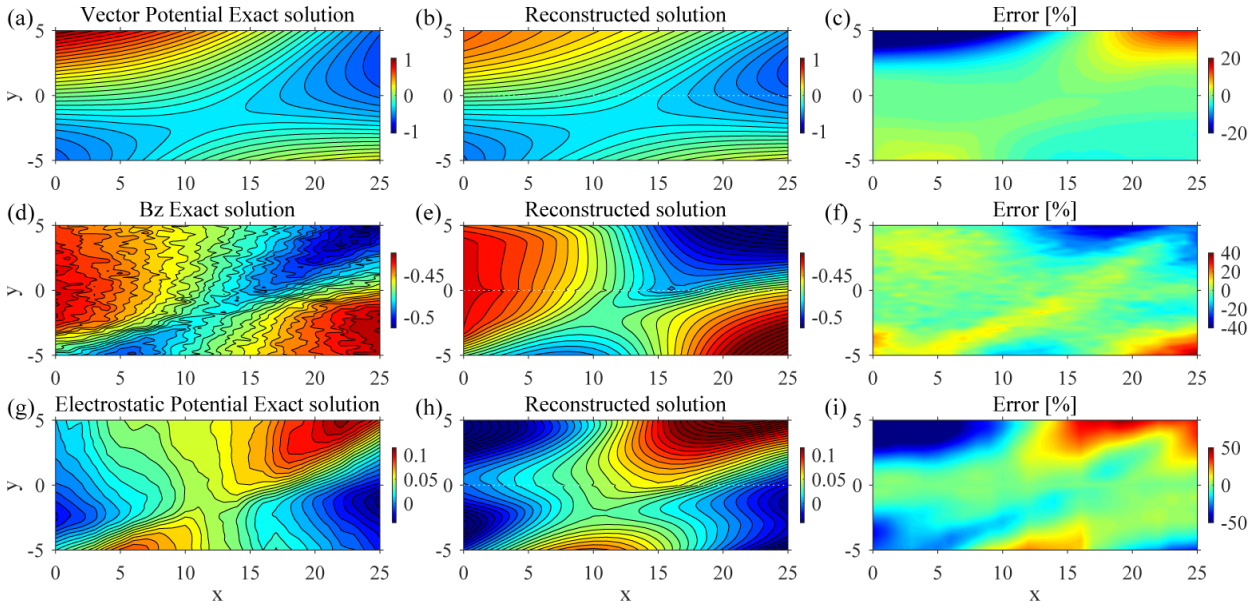

Figure 5. Results from the incompressible finite-inertia version "in,Case-2", applied to data from PIC simulation of guide-field reconnection. The format is the same as in Figure 2, but only for A, B_z, and ϕ. The B_z error here is defined to be $\frac{(B_{z,rcstr}-B_{z,sim})}{(B_{z,sim,max}-B_{z,sim,min})}$, where subscripts "rcstr", "sim", "max", and "min" represent the reconstructed, simulation, maximum, and minimum values, respectively.

It should be pointed out that the reconstructed $B_z(x, y)$ (Figure 5e) is good enough, despite the fact that only Case 2 (Hesse-Kuznetsova dissipation term for antiparallel reconnection) is used in the B_z integration. The results from the combined Cases 1 and 2 version "in,Case-1&2" and from the compressible version are similar to those shown in Figure 5, but have slightly larger errors on average (see Figure S4 for the plots of errors from the variants of the EMHD code in the guide-field reconnection case, corresponding to Figure 3 in the antiparallel reconnection case). The larger errors for the compressible case is possibly because in the presence of significant guide field, the electron density is not even approximately preserved along the transverse field lines (Pritchett & Coroniti, 2004; Le et al., 2010), violating the present model assumption $n = n(A)$. We also note that Hesse et al. (2011) give an expression for $f(L, N)$ in the case of guide-field reconnection as well, but we could not incorporate it into our reconstruction code because of numerical difficulties. In summary, the test results demonstrate that our newly developed EMHD code can reconstruct general properties of the magnetic field, electron velocity, and electrostatic potential in and around the EDR of guide-field as well as antiparallel reconnection.

5 Application to MMS Data

As a demonstration that the new EMHD code works for actual observations, the incompressible, finite-inertia version with Case 2 only has been applied to MMS observations of a magnetotail EDR on 11 July 2017, 2234:01.7 0.1–2234:03.1 UT. This EDR is of nearly antiparallel, symmetric reconnection, and was previously studied by Torbert et al. (2018) and reconstructed with the original EMHD code by Hasegawa et al. (2019), hereafter referred to as H19. In this event, the MMS3 spacecraft was located at (–21.6, 4.2, 3.6) R_E in the geocentric solar ecliptic (GSE) coordinate system. Magnetic field and electron moment data used to set the initial conditions are from the fluxgate magnetometers (FGM) (Russell et al., 2016) and Fast Plasma Investigation (FPI) instruments (Pollock et al., 2016), respectively. The coordinate axes, structure velocity, function $v_z(A)$, and reconnection electric field E_{z0} used in the reconstruction are exactly the same as optimized and used by H19 (see Table S1 of their paper). The only difference in the initial conditions is that the x component of the electron convection electric field $E_{cx} = -(\mathbf{v} \times \mathbf{B})_x$ in the structure frame is used to compute the electrostatic potential $\phi(x, 0)$ along the spacecraft path in the present study, while in H19 it is not used but ϕ is computed from (25) in S16.

Figure 6 shows the maps of the magnetic field, electron velocity, and electrostatic potential ϕ reconstructed by the incompressible, finite-inertia version of our new EMHD code from the data taken by MMS3 that approached closest to the X point (the field maps from the other three spacecraft are included as Figures S5-S7 in the Supporting Information). The results were not improved by use of the compressible version, probably because the electron density and temperature were both approximately constant in the present event (Figure 2 of H19), well satisfying the incompressibility assumption. The reconstructed transverse field lines are very similar to those from the S16 version (see Figure 4a of H19), while the electron streamlines are more or less symmetric with respect to the electron stagnation point located at $(x, y) \sim (230, -10)$ km, in stark contrast with the unrealistic skewed pattern of the streamlines reconstructed by H19 (their Figure 4b). Consistent with the earlier result (H19), the stagnation point is displaced ~90 km, about three times the electron inertial length ($\lambda_e \sim 27$ km), in the earthward direction from the reconstructed X point. In the normal direction, on the other hand, one may conclude that the stagnation point is near the center of the current sheet, on the assumption that the position error is at most λ_e when the reconstructed stagnation point is located within ~$2\lambda_e$ of the spacecraft path $y = 0$ (Figure 5; Sonnerup et al., 2016). The out-of-plane field component B_z at the stagnation point is nearly zero, consistent with near antiparallel reconnection with no or only a weak guide field component. The ϕ map is also consistent with the previous study (Figure 4c of H19), with a potential minimum at the central portion of the reconnecting current sheet.

Figure 7 shows scatter plots of the three GSE components of the magnetic field, electron velocity, and electric field (in the structure frame) predicted from the MMS3 maps (Figure 6) at points along the paths of the other three spacecraft (MMS1, MMS2, and MMS4) and those actually measured by MMS. Here, the measured electric field data are from the double-probe instruments (Lindqvist

et al., 2016; Ergun et al., 2016), not of the electron convection. The bootstrap method (e.g., Kawano & Higuchi, 1995) is used to estimate the confidence intervals of the correlation coefficients corresponding to ± 1 sigma. The correlation coefficient (0.9945) for the magnetic field is nearly equal to that (0.9942) obtained by H19, indicating a sufficient accuracy of the reconstructed magnetic field. The correlation coefficient (0.9646) for the electron velocity (Figure 7b) is slightly higher than that obtained by H19 (0.9632). This is an improvement from including the inertia term (the last term on the right-hand side of (17)), because by disabling this term the correlation coefficient becomes lower. In this particular event, the electron beta $\beta_e = \frac{n_0 k T_{e0}}{\left(\frac{B_0^2}{(2\mu_0)}\right)}$ was high (~2), where n_0 and T_{e0} are the mean electron density and temperature, respectively, and B_0 is the magnitude of the reconnecting field component, so that on average the inertia term contribution must have been smaller than that of the electron pressure tensor term. Note, however, that the exact contribution of each term in the Generalized Ohm's law to the reconnection electric field E_0 depends on the location in the reconnection region (e.g., Figure 2 of Divin et al., 2012; Figure 4 of Egedal et al., 2019).

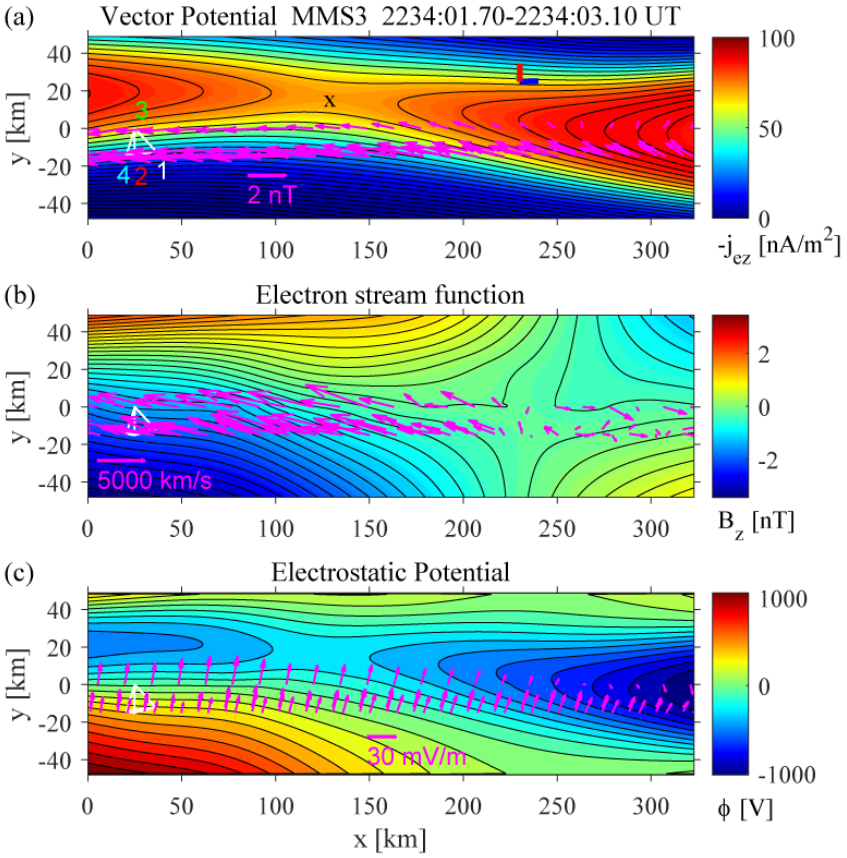

Figure 6. Results from the incompressible, finite-inertia version "in,Case-2 only" of the EMHD reconstruction, applied to MMS3 observations of the magnetotail EDR on 11 July 2017 (Torbert et al., 2018). The figure is equivalent to Figure 4 of Hasegawa et al. (2019), except for different color coding (the magenta arrows are the projections onto the reconstruction plane of the measured components of (a) the magnetic field, (b) electron velocity, and (c) electric field in the structure frame. The measured electric field data were obtained by the double-probe instruments (Lindqvist et al., 2016; Ergun et al., 2016). The blue, green, and red bars the projections of the unit vectors of the GSE x, y, and z axes (the green bar is barely visible). GSE components of the reconstruction axes are: $\hat{\mathbf{x}}$ = (0.9950, –0.0979, 0.0178), $\hat{\mathbf{y}}$ = (0.0143, 0.3174, 0.9482), and $\hat{\mathbf{z}}$ = (–0.0985, –0.9432, 0.3172).

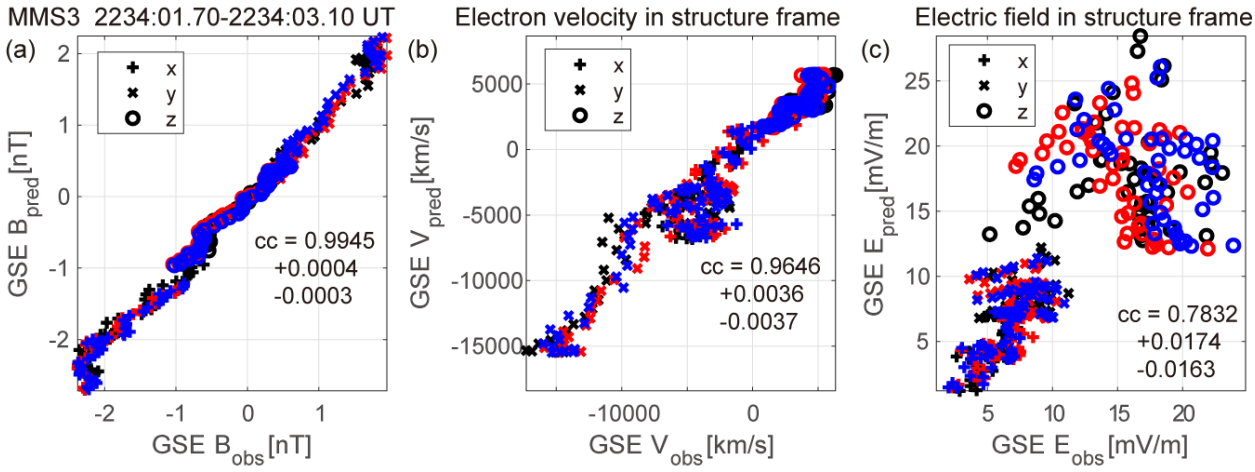

Figure 7. Scatter plots of the predicted and observed values of the GSE components of (a) the magnetic field, (b) electron velocity, and (c) electric field, corresponding to Figures 5j-5l of H19. The black, red, and blue points are the data from MMS1, MMS2, and MMS3, respectively.

The correlation coefficient for the electric field ($\mathrm{cc}_E = 0.7832$) is slightly higher than that (0.7816) obtained by H19. In summary, the magnetic field, electric field, and electron velocity field are all better reconstructed by the new EMHD code than the inertia-less version (S16). Table S1 gives a summary of reconstruction results from each of the four MMS spacecraft, which demonstrates that the performance of the new EMHD code is comparable or better than the S16 code in recovering the magnetic field, electric field, and electron velocity structures. The table also includes cc_E in the case when $\phi(x, 0)$ is computed from E_x measured by the double-probe instruments, which are comparable to cc_E based on the use of $E_{cx} = -(\mathbf{v} \times \mathbf{B})_x$.

6 Summary and Discussion

We have extended a method based on electron magnetohydrodynamics (EMHD)

to reconstruct 2-D plasma and magnetic field structures in and around the EDR from data taken by a single spacecraft, originally developed by Sonnerup et al. (2016). Contrary to the original method, the new method accommodates nonuniform density and temperature (compressibility), finite electron inertia, and guide magnetic field in the reconnection region, and thus has more applicability. It has been successfully benchmarked by use of results from fully kinetic simulations of both antiparallel and guide-field reconnection, with generally smaller errors than from the original one. It has further been applied to an EDR of magnetotail reconnection observed by the MMS spacecraft on 11 July 2017 (Torbert et al., 2018; Hasegawa et al., 2019), and a better performance in reconstructing the electric field and electron velocity structure has been demonstrated.

One significant advantage of our new method is that Case 1 for the streamline (B_z) reconstruction does not require any model for the off-diagonal terms of the electron pressure tensor in the EDR (section 3.2.1), so that it is applicable to guide-field as well as antiparallel reconnection. While it was confirmed in section 4.2 that the Hesse-Kuznetsova dissipation term for antiparallel reconnection (Case 2) is sufficiently good in the case of the guide field intensity comparable to that of the reconnecting field, the use of Case 1 may be needed for reconnection with a very intense guide field, as observed in the turbulent magnetosheath (Phan et al., 2018). Even in such cases, Case 2 will have to be used in the part of the reconstruction domain where $|v_y|$ in the reconstruction coordinate system is very small.

One issue that needs to be addressed in applications to guide-field reconnection is that in the presence of strong guide field, the electron density cannot be a function of A only (Pritchett and Coroniti, 2004; Le et al., 2010), i.e., the density is lower around the separatrices with larger B_z (Hall plus guide field) magnitude than around the other separatrices (Figure 5d), so that the density varies substantially along the transverse field lines around the separatrices. In such situations, $n(A)$ (and probably $p(A)$ also) should be modeled to have double branches, one for two of the four Hall-field quadrants with positive B_z perturbations and one for the other two quadrants with negative B_z perturbations. The double-branch fitting would require observations in which single or multiple spacecraft traverse both quadrants with positive and negative B_z perturbations, and reconstruction using double branches will be attempted in the future.

The newly developed compressible EMHD code could be applicable to highly asymmetric reconnection, as observed at the magnetopause (Burch and Phan, 2016), as well as to approximately symmetric reconnection to which the incompressible S16 code has been applied (Hasegawa et al., 2017, 2019). Since magnetopause current layers have a higher density and lower temperature on the magnetosheath side than on the magnetospheric side (Burch and Phan, 2016), different functional behaviors of both $n(A)$ and $p(A)$ are expected for the magnetosheath and magnetospheric sides, even in the absence of the guide field. Note that the magnetosheath and magnetospheric regions on the inflow

side of the separatrix magnetic flux surfaces are on different field lines, but can have an equal A value. In such situations, the functional forms should be determined separately for the magnetosheath and magnetospheric sides, by separating the input data by the polarity of B_L ($B_L < 0$ on the magnetosheath side and $B_L > 0$ on the magnetospheric side). This type of double-branch fitting technique was first developed by Hu and Sonnerup (2003) in applications of the magnetohydrostatic GS reconstruction to magnetopause crossings.

It may be helpful to discuss how the reconstruction of one quantity is coupled to or decoupled from that of others. By use of (18), the reconstruction of the transverse magnetic field (A) is independent of that of the in-plane velocity field (B_z) and electrostatic potential (ϕ). This explains why A is recovered so accurately that the A error is much smaller than those of B_z and ϕ (Figure 3). On the other hand, it is seen from (21) that the B_z reconstruction in Case 1 depends on how accurately both A and ϕ (or G) are reconstructed, while from (24) the B_z reconstruction in Case 2 is coupled to that of A, but is decoupled from that of ϕ (or G). As for the ϕ (or G) reconstruction, it is seen from (25) that it is coupled to both the A and B_z reconstructions. Thus, the lower correlation coefficient for the electric field in the application to the MMS event (Figure 7c) may be a combined effect of not completely accurate reconstruction of A and B_z and less accurate measurements of the electric field by the double-probe instruments or through the use of the convection electric field (as compared to the magnetic field measurements) that can lead to larger error in the ϕ reconstruction.

While electron beta β_e was relatively high (~2) in the magnetotail EDR event on 11 July 2017, magnetotail reconnection can occur under lower beta conditions, especially during intense substorms (Nagai et al., 1998). For lower beta cases the inertia terms (terms with m_e in (10) and (17)) make a larger contribution to the electron momentum equation, and a larger difference is expected in the streamlines reconstructed with the inertia-less (S16) and finite-inertia EMHD codes. However, low beta events should be analyzed with care, because when β_e is low the density is often low, so that electron moment data may become less reliable because of lower counting statistics. A comparison of the EDR structure and energy conversion process between higher and lower beta cases is an interesting topic that needs to be addressed in a future study of more events from the MMS mission.

Appendix: Assumptions on $\mathbf{^2A}$ and $\mathbf{^2B_z}$

In the present reconstruction, it is assumed that $\nabla^2 A$, or equivalently nv_z under negligible ion and displacement currents, can be expressed as a function of A only. We assess whether this assumption is a good approximation in a 2-D fully kinetic simulation of antiparallel magnetic reconnection (Nakamura et al., 2016). Figure A1 shows that although nv_z is not strictly preserved along the transverse field lines and that on a selected field line is larger at locations closer to the X point, nv_z may be approximated as a function of A only. On the other hand, $\nabla^2 B_z$ can be a function of neither A nor B_z only, contrary to the assumption

made by Korovinskiy et al. (2021) in their Model 2 or 1, respectively.

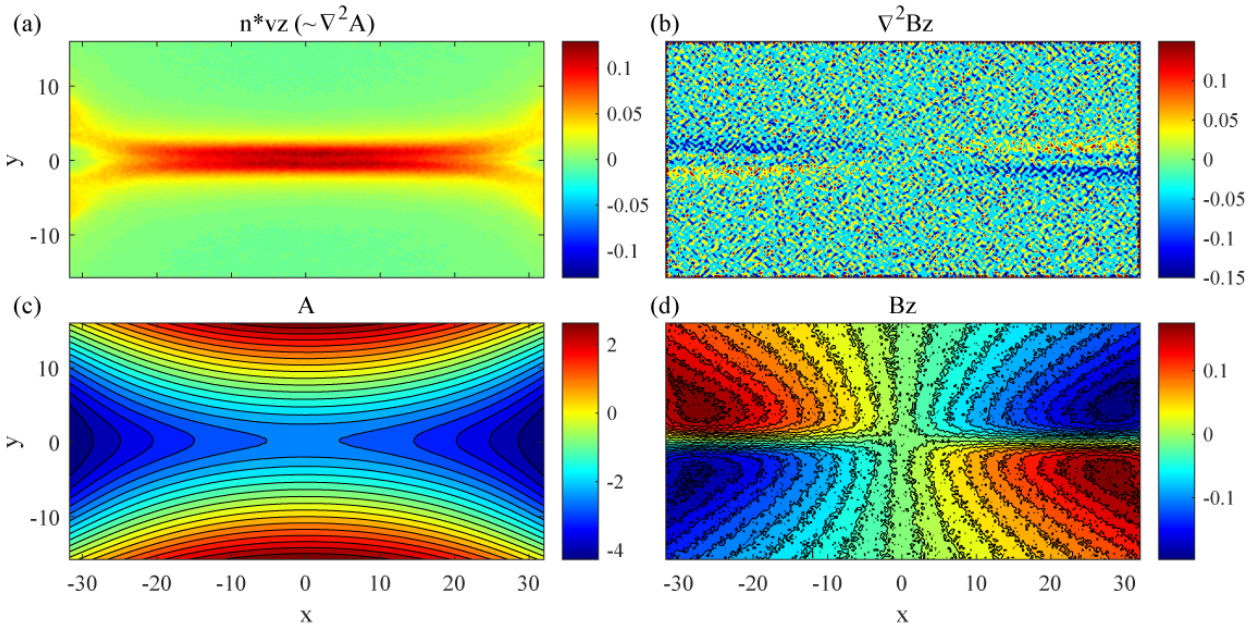

Figure A1. (a) nv_z, (b) $\nabla^2 B_z$ (c) A and (d) B_z in the xy plane from the 2-D fully kinetic simulation of symmetric, antiparallel magnetic reconnection (Nakamura et al., 2016). The coordinates are normalized to the electron inertial length λ_{e0}.

Another interesting feature seen in the simulation is that the magnitude of $\nabla^2 B_z$ is significantly large only in the regions close to the center of the current sheet (Figure A1b). Taking advantage of this feature, our reconstruction imposes $\nabla^2 B_z = 0$ in the part of the reconstruction domain where the magnitude of the transverse magnetic field $B_\perp$ is larger than a threshold value (~0.5 in the normalized unit) and the magnitude of $\frac{\partial^2 B_z}{\partial y^2}$ based on (21) when Case 1 is used or (24) when Case 2 is used exceeds a threshold value (~0.1 in the normalized unit), so that $\frac{\partial^2 B_z}{\partial y^2} = -\frac{\partial^2 B_z}{\partial x^2}$ is used in such a domain.

Finally, we summarize the key differences between our new EMHD method and reconstruction models developed by Korovinskiy et al. (2021). In their Model 1 $\nabla^2 B_z$ is taken to be a function of B_z only (their Eq. (18)), while in their Model 2 $\nabla^2 B_z$ is a function of A only (their Eq. (22)). On the other hand, such a strong constraint is not imposed in our EMHD method by use of (21) where G is a function of both A and B_z (see (14) and (15)). Their Model 3 is somewhat similar to our Case 2 (section 3.2.2), but their model assumes incompressible electrons (n = const. and T_e = const.) and negligible electron inertia, while our Case 2 includes the effects of both finite electron inertia and spatial inhomogeneity of the electron density and temperature (see (24)).

Acknowledgments, and Data

The MMS data are available from the MMS Science Data Center: https://lasp.colorado.edu/mms/sdc/public/. The present study used version 3.3 of the FPI burst-mode data. Data access and processing was done using SPEDAS V4.1 (Angelopoulos et al., 2019): http://spedas.org/blog/. The Matlab code for the new EMHD reconstruction can be found at the Zenodo (https://doi.org/10.5281/zenodo.5144478). The work by H.H. was supported by JSPS Grant-in-aid for Scientific Research KAKENHI 21K03504. T.K.M.N. was supported by the Austrian Research Fund (FWF): P32175-N27. R.E.D. was supported by NASA grant 80NSSC19K0254.

References

Angelopoulos, V., Cruce, P., Drozdov, A., Grimes, E. W., Hatzigeorgiu, N., King, D. A., et al. (2019). The Space Physics Environment Data Analysis System (SPEDAS). *Space Science Reviews*, *215*, 9. https://doi.org/10.1007/s11214-018-0576-4.

Chen, W., Wang, X., Tsyganenko, N. A., Andreeva, V. A., & Semenov, V. S. (2019). Reconstruction of local magnetic structures by a modified radial basis function method. *Journal of Geophysical Research: Space Physics*, 124, 10141–10152. https://doi.org/10.1029/2019JA027078.

Burch, J. L., Torbert, R. B., Phan, T. D., Chen, L. J., et al. (2016). Electron-scale measurements of magnetic reconnection in space. *Science*, 352, aaf2939. doi:10.1126/science.aaf2939.

Burch, J. L., & Phan, T. D. (2016). Magnetic reconnection at the dayside magnetopause: Advances with MMS. *Geophys. Res. Lett.*, 43, 8327–8338. doi:10.1002/2016GL069787.

Denton, R. E., Sonnerup, B. U. Ö., Hasegawa, H., Phan, T.-D., Russel, C. T., Strangeway, R. J., Giles, B. L., Gershman, D. J., & Torbert, R. B. (2016). Motion of the MMS Spacecraft Relative to the Magnetic Reconnection Structure Observed on 16 Oct2015 at 1307 UT. *Geophys. Res. Lett.*, 43, 5589–5596. doi:10.1002/2016GL069214.

Denton, R. E., Sonnerup, B. U. Ö., Russell, C. T., Hasegawa, H., Phan, T.-D., Strangeway, R. J., et al. (2018). Determining L-M-N current sheet coordinates at the magnetopause from Magnetospheric Multiscale data. *Journal of Geophysical Research: Space Physics*, 123, 2274–2295. https://doi.org/10.1002/2017JA024619.

Denton, R. E., Torbert, R. B., Hasegawa, H., Dors, I., Genestreti, K. J., Argall, M. R., et al. (2020). Polynomial reconstruction of the reconnection magnetic field observed by multiple spacecraft. *Journal of Geophysical Research: Space Physics*, 125, e2019JA027481. https://doi.org/10.1029/2019JA027481.

Denton, R. E., Torbert, R. B., Hasegawa, H., Genestreti, K. J., Manuzzo, R., Belmont, G., et al. (2021). Two-dimensional velocity of the magnetic structure

observed on 11 July 2017 by the Magnetospheric Multiscale spacecraft. *J. Geophys. Res. Space Physics*, 126, e2020JA028705. https://doi.org/10.1029/2020JA028705.

Divin, A., Lapenta, G., Markidis, S., Semenov, V. S., Erkaev, N. V., Korovinskiy, D. B., & Biernat, H. K. (2012). Scaling of the inner electron diffusion region in collisionless magnetic reconnection, *J. Geophys. Res.*, 117, A06217. doi:10.1029/2011JA017464.

Egedal, J., Ng, J., Le, A., Daughton, W., Wetherton, B., Dorelli, J., Gershman, D., & Rager, A. (2019). Pressure tensor elements breaking the frozen-in law during reconnection in Earth's magnetotail. *Phys. Rev. Lett.*, 123, 225101. doi:10.1103/PhysRevLett.123.225101.

Ergun, R. E., Tucker, S., Westfall, J., Goodrich, K. A., Malaspina, D. M., Summers, D., et al. (2016). The axial double probe and fields signal processing for the MMS mission. *Space Science Reviews*, *199*(1-4), 167–188. https://doi.org/10.1007/s11214-014-0115-x.

Hasegawa, H., Sonnerup, B. U. Ö., Denton, R. E., et al. (2017). Reconstruction of the electron diffusion region observed by the Magnetospheric Multiscale spacecraft: First results. *Geophys. Res. Lett.*, 44, 4566–4574. doi:10.1002/2017GL073163.

Hasegawa, H., Denton, R. E., Nakamura, R., Genestreti, K. J., Nakamura, T. K. M., Hwang, K.-J., et al. (2019). Reconstruction of the electron diffusion region of magnetotail reconnection seen by the MMS spacecraft on 11 July 2017. *Journal of Geophysical Research: Space Physics*, 124, 122–138. https://doi.org/10.1029/2018JA026051.

Hau, L.-N., & Sonnerup, B. U. Ö. (1999). Two-dimensional coherent structures in the magnetopause: Recovery of static equilibria from single-spacecraft data. *J. Geophys. Res.*, 104(A4), 6899–6917. doi:10.1029/1999JA900002.

Hesse, M., Neukirch, T., Schindler, K., Kuznetsova, M., & Zenitani, S. (2011). The diffusion region in collisionless magnetic reconnection. *Space Sci. Rev.*, 160, 3–23. doi:10.1007/s11214-010-9740-1.

Hu, Q., & Sonnerup, B. U. Ö. (2003). Reconstruction of two-dimensional structures in the magnetopause: Method improvements. *J. Geophys. Res.*, 108(A1), 1011. doi:10.1029/2002JA009323.

Kawano, H. & Higuchi, T. (1995). The bootstrap method in space physics: Error estimation for minimum variance analysis. *Geophys. Res. Lett.*, 22, 307–310, doi:10.1029/94GL02969.

Korovinskiy, D. B., Divin, A. V., Semenov, V. S., Erkaev, N. V., Kiehas, S. A., and Kubyshkin, I. V. (2020). Grad-Shafranov reconstruction of the magnetic configuration in the reconnection X-point vicinity in compressible plasma. *Phys. Plasmas*, 27, 082905. https://doi.org/10.1063/5.0015240.

Korovinskiy, D. B., Kiehas, S. A., Panov, E. V., Semenov, V. S., Erkaev, N. V., Divin, A. V., & Kubyshkin, I. V. (2021). The inertia-based model for reconstruction of the electron diffusion region. *Journal of Geophysical Research: Space Physics*, 126, e2020JA029045. https://doi.org/10.1029/2020JA029045.

Le, A., Egedal, J., Fox, W., Katz, N., Vrublevskis, A., Daughton, W., & Drake, J. F. (2010). Equations of state in collisionless magnetic reconnection. *Phys. Plasmas*, 17, 055703. doi:10.1063/1.3309425.

Lindqvist, P.-A., Olsson, G., Torbert, R. B., King, B., Granoff, M., Rau, D., et al. (2016). The spin-plane double probe electric field instrument for MMS. *Space Science Reviews*, *199*(1-4), 137–165. https://doi.org/10.1007/s11214-014-0116-9.

Nagai, T., Fujimoto, M., Saito, Y., Machida, S., Terasawa, T., Nakamura, R., Yamamoto, T., Mukai, T., Nishida, A., & Kokubun, S. (1998). Structure and dynamics of magnetic reconnection for substorm onsets with Geotail observations. *J. Geophys. Res.*, 103(A3), 4419–4440. doi:10.1029/97JA02190.

Nakamura, T. K. M., Nakamura, R., & Hasegawa, H. (2016). Spatial dimensions of the electron diffusion region in anti-parallel magnetic reconnection. *Ann. Geophys.*, 34, 357–367. doi:10.5194/angeo-34-357-2016.

Nakamura, T. K. M., Hasegawa, H., Genestreti, K. J., Denton, R. E., Phan, T. D., Stawarz, J. E., et al. (2021). Fast cross-scale energy transfer during turbulent magnetic reconnection. *Geophysical Research Letters*, 48, e2021GL093524. https://doi.org/10.1029/2021GL093524.

Phan, T. D., Eastwood, J. P., Shay, M. A., Drake, J. F., Sonnerup, B. U. Ö., et al. (2018). Electron magnetic reconnection without ion coupling in Earth's turbulent magnetosheath. *Nature*, 557, 202–206. doi:10.1038/s41586-018-0091-5.

Pollock, C., Moore, T., Jacques, A., Burch, J., Gliese, U., Saito, Y., et al. (2016). Fast Plasma Investigation for Magnetospheric Multiscale. *Space Science Reviews*, *199*(1-4), 331–406. https://doi.org/10.1007/s11214-016-0245-4.

Pritchett, P. L., & Coroniti, F. V. (2004). Three-dimensional collisionless magnetic reconnection in the presence of a guide field. *J. Geophys. Res.*, 109, A01220. doi:10.1029/2003JA009999.

Russell, C. T., Anderson, B. J., Baumjohann, W., Bromund, K. R., Dearborn, D., Fischer, D., et al. (2016). The Magnetospheric Multiscale Magnetometers. *Space Science Reviews*, *199*(1-4), 189–256. https://doi.org/10.1007/s11214-014-0057-3.

Sonnerup, B. U. Ö., Hasegawa, H., Teh, W.-L., & Hau, L.-N. (2006). Grad-Shafranov reconstruction: An overview. *J. Geophys. Res. Space Physics*, 111, A09204. doi:10.1029/2006JA011717.

Sonnerup, B. U. Ö., Hasegawa, H., Denton, R. E., & Nakamura, T. K. M. (2016).

Reconstruction of the electron diffusion region. *J. Geophys. Res. Space Physics*, 121, 4279–4290. doi:10.1002/2016JA022430.

Shi, Q. Q., Tian, A. M., Bai, S. C., Hasegawa, H., Degeling, A. W., Pu, Z. Y., Dunlop, M., Guo, R. L., Yao, S. T., Zong, Q.-G., Wei, Y., Zhou, X.-Z., Fu, S. Y., & Liu, Z. Q. (2019). Dimensionality, coordinate system and reference frame for analysis of in-situ space plasma and field data. *Space Sci. Rev.*, 215, 35. https://doi.org/10.1007/s11214-019-0601-2.

Torbert, R. B., Burch, J. L., Phan, T. D., ... Saito, Y. (2018). Electron-scale dynamics of the diffusion region during symmetric magnetic reconnection in space. *Science*, 362, 1391-1395. doi:10.1126/science.aat2998.

Torbert, R. B., Dors, I., Argall, M. R., Genestreti, K. J., Burch, J. L., Farrugia, C. J., et al. (2020). A new method of 3-D magnetic field reconstruction. *Geophysical Research Letters*, 47, e2019GL085542. https://doi.org/10.1029/2019GL085542.